applied sciences

MDPI

Article

Detectability of Coseismic Offsets and Early Post-Event Coordinate Changes from Public GNSS Products: The 2024 Mw 7.4 Hualien Earthquake

Guobing Liang [1], Maosheng Zhang [2,3,*], Li Feng [2], Ying Dong [3] and Yuteng Yan [2]

[1] School of Geological Engineering and Geomatics, Chang'an University, Xi'an 710054, China; liangguobing@chd.edu.cn
[2] School of Human Settlements and Civil Engineering, Xi'an Jiaotong University, Xi'an 710049, China; fengli726@xjtu.edu.cn (L.F.); yuna.yan5@stu.xjtu.edu.cn (Y.Y.)
[3] Key Laboratory of Loess Geological Hazards, Ministry of Natural Resources, Xi'an 710119, China; dongy@mail.cgs.gov.cn
* Correspondence: xjtzms@xjtu.edu.cn

Abstract

Public Global Navigation Satellite System (GNSS) products offer rapid access to earthquake deformation, but sparse sampling and shared processing constrain the interpretation of short records. We evaluate the 2024 Mw 7.4 Hualien earthquake using official coseismic offsets, five-minute positions, and daily coordinate series. Fixed-window estimates recover the main coseismic displacement pattern, providing a product-consistency check rather than independent validation. Spatial-block resampling reveals substantial uncertainty in the vertical cross-product comparison. For the first fortnight, we compare constant, linear, logarithmic, and exponential descriptions and distinguish nonconstant variation from resolvable curvature. The linear alternative is essential: most screened coordinate changes do not require a curved transient. Ten components retain screened status under the tested stability, seasonal/step, and common-mode diagnostics, but this conditional retention does not establish a physical deformation mechanism. Under the specified correlated-noise experiment, the intermediate-screen count is not unusual (exceedance probability 0.255); this experiment does not calibrate the complete final-retention procedure. Public products therefore provide useful coseismic consistency information, whereas short-record post-event changes remain sensitive to background treatment and cannot establish a spatially coherent postseismic mechanism.

Keywords: Hualien earthquake; coseismic displacement; five-minute GNSS; daily GNSS; coordinate changes; corrected Akaike information criterion

Check for updates

Academic Editor: Cristina Sáez Blázquez

Received: 19 September 2026
Revised: 21 October 2026
Accepted: 22 October 2026
Published: 26 October 2026

Copyright: © 2026 by the authors. Licensee MDPI, Basel, Switzerland. This article is an open access article distributed under the terms and conditions of the Creative Commons Attribution (CC BY) license.

1. Introduction

The Mw 7.4 Hualien earthquake occurred at 23:58:12 Coordinated Universal Time (UTC) on 2 April 2024 (07:58 local time on 3 April) near the northern Longitudinal Valley of eastern Taiwan. This region marks a rapid transition from oblique collision between the Philippine Sea and Eurasian plates to subduction northeast of Taiwan. Regional deformation is partitioned among the Longitudinal Valley fault, the Central Range fault, offshore backthrusts, and deeper plate-boundary structures [1–7]. Consequently, the inferred fault geometry depends in part on the observations and modeling assumptions used. Land geodesy, joint seismic-geodetic inversion, seafloor geodesy, and tsunami observations resolve different parts of the rupture and have supported east-dipping, west-dipping, and

multifault interpretations [8–12]. The event therefore provides a useful opportunity to assess what can be established directly from public geodetic products before introducing a new source inversion.

Global Navigation Satellite System (GNSS) products sampled at different temporal resolutions do not necessarily resolve the same quantities. An official coseismic-offset solution estimates a static displacement step within a network-processing framework. A subdaily position series indicates whether an abrupt coordinate change is resolved near the earthquake origin time and how its estimated magnitude depends on the selected observation window. A daily position series is better suited to assessing continued motion after the event, but the first few weeks contain relatively few observations and may be affected by temporally correlated errors. Moreover, products derived from shared stations, orbit products, and reference-frame realizations are not statistically independent simply because their sampling intervals differ [13–18]. Comparisons between such products should therefore be interpreted as assessments of cross-product consistency rather than as independent validation. Their agreement also needs to be evaluated using component-wise bias, absolute error, concordance, and errors-in-variables regression rather than Pearson correlation alone.

Earlier GNSS studies distinguish the estimation of an earthquake step from the characterization of subsequent deformation. The Detection of Offsets in GPS (Global Positioning System) Experiment (DOGEx) benchmarks offset detection against known synthetic discontinuities and demonstrates the influence of noise and unmodeled changes [19]. Tobita [20] compares logarithmic and exponential functions, steady velocities, and multi-timescale combinations using a two-year postseismic fitting interval; that approach has far more curvature information than a first-fortnight record. Correlated-noise likelihood methods jointly estimate deterministic terms and stochastic structure [21,22], while regional spatial filtering addresses common-mode contributions [23,24]. These approaches motivate explicit background and linear controls in a short-record assessment. The methodological gap addressed here is a provider-file-to-result audit that separates support for any nonconstant variation from evidence of resolvable curvature in a sparse public daily record. Rapid coseismic studies [25,26] address recovery of earthquake displacement, whereas afterslip and longer-lived postseismic studies [27–34] provide physical interpretations supported by source geometry or longer observations. Those objectives differ from short-record model discrimination, but explain why empirical curvature alone cannot establish a relaxation mechanism.

Published multisensor rupture studies provide structural context through GNSS, interferometric synthetic aperture radar (InSAR), seismic, seafloor, and tsunami observations [8–12]. Their observables and model parameters are kept distinct in this study: a GNSS component or vector norm, a radar line-of-sight displacement, fault slip, and initial sea-surface elevation are different physical quantities. The literature comparison summarizes the observation types and inferred geometry without using peak amplitudes as numerical agreement tests. The U.S. Geological Survey (USGS) finite-fault overlay is retained as Supplementary Figure S1 for geographic orientation.

The assessment distinguishes directly observed product quantities, model support conditional on an analysis procedure, and physical attribution. Coseismic product consistency is evaluated with absolute differences and errors-in-variables regression. Daily-coordinate variation is evaluated against both constant and linear alternatives, then subjected to background and sampling diagnostics. A selected empirical curve summarizes the available observations; interpretation as a particular deformation process requires additional temporal and spatial constraints.

The study asks how public five-minute positions recover official coseismic offsets, how much short daily records support nonconstant or curved behavior, and which results persist

across reasonable analysis choices. Its contribution is the assessment of temporal-resolution effects, background sensitivity, and the limits of empirical model selection, together with a reproducible workflow. The official displacement field supplies the observational reference for that assessment.

2. Data and Tectonic Context

2.1. Public Data Inventory

All inputs were downloaded from public providers and retained under their original filenames. The primary datasets comprise official Nevada Geodetic Laboratory (NGL) coseismic offsets, compressed NGL 5-min final KENV position series, and daily NGL TENV3 position series. The USGS event page and finite-fault product, together with the Advanced National Seismic System Comprehensive Earthquake Catalog (ANSS ComCat), were used only to provide event and regional seismicity context. Plate boundaries, active faults, coastlines, and topography were obtained from the PB2002 plate-boundary model, the Global Earthquake Model (GEM) Global Active Faults Database, Natural Earth, and the Earth Topography 2022 (ETOPO 2022) model, respectively [35–37]. The data manifest records the source uniform resource locator (URL), access date, original filename, file size, and 256-bit Secure Hash Algorithm (SHA-256) digest for each of the 222 provider files. Table 1 summarizes the datasets and their analytical roles.

The official offsets provide the reference static field; five-minute KENV records support event-window consistency checks; and daily TENV3 records support first-fortnight coordinate analysis. Most retained daily provider files end on 16 April 2024. This is the endpoint of the frozen archive used here, rather than a claim that later public observations do not exist. The fixed first-fortnight interval evaluates an early-information setting. Ninety-nine files contain at least ten observations in this interval and 101 contain at least eight. HUAP has only one observation during days 1–7 and fails the three-sample preprocessing requirement, leaving 100 stations and 300 components for baseline model comparison (Figure 1). Longer pre-event histories within the same files are used for the seasonal-background diagnostic. No later daily solution is merged into the frozen first-fortnight analysis.

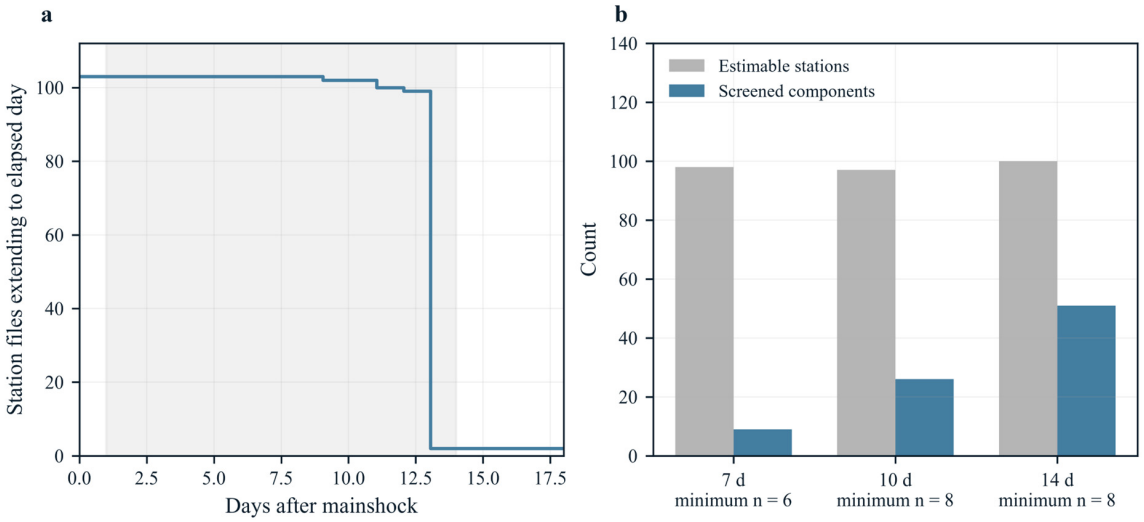


Figure 1. Frozen daily archive coverage and revised fit eligibility. (**a**) Number of station files extending to each elapsed day; the shaded interval marks days 1–14. (**b**) Gray bars show estimable stations within the retained baseline network, and blue bars show intermediate-screen station-components, so the two series use different counting units. Seven-day fits require at least six observations; ten- and fourteen-day fits require at least eight. Baseline records contain 8–13 epochs within days 1–14. Here n denotes the number of retained daily observations. Not-estimable components are reported separately from fitted components.

Table 1. Public data sources and their analytical roles. Dataset abbreviations: NGL, Nevada Geodetic Laboratory; USGS, U.S. Geological Survey; ANSS ComCat, Advanced National Seismic System Comprehensive Earthquake Catalog; PB2002, plate-boundary model of Bird [35]; GEM, Global Earthquake Model; ETOPO, Earth Topography. KENV and TENV3 are provider position-file format identifiers.

Dataset	Scale	Role
NGL official coseismic offsets	105 stations	Reference static displacement field
NGL 5 Minute Final KENV	103 station archives	1-, 3-, and 6-h event-window consistency
NGL daily TENV3	105 station files	Pretrend and days 1-14 transient detectability
USGS finite-fault product	Published event product	Contextual rupture overlay only
USGS ANSS ComCat	396 downloaded events	Regional map background only
PB2002, GEM, Natural Earth, ETOPO 2022	Regional layers	Plate, fault, coastline, and relief context

2.2. Regional Setting and Published Rupture Interpretations

The northern Longitudinal Valley is a double-vergent suture characterized by steep relief and closely spaced active structures. Historical, geological, and geodetic studies indicate that deformation is partitioned among valley-bounding faults and structures beneath the Central Range and offshore domain [38–41]. Source studies of the 2013 Ruisui and 2009 Fengpin–Hualien earthquake sequences further demonstrate that local rupture interpretations are sensitive to fault geometry and to the type of data analyzed [42,43].

This structural ambiguity remains evident for the 2024 event. Cheloni et al. [8] combined GNSS and InSAR observations to infer a composite source and reported approximately 0.40–0.45 m of maximum line-of-sight deformation near Hualien. Qiu et al. [44] combined InSAR and GNSS observations but favored a west-dipping structure, whereas Zheng et al. [45] inferred a blind listric, southeast-dipping thrust. Broader seismogeodetic analyses by Xu et al. [46] and Liu et al. [9] instead resolved conjugate participation. These differences concern more than dip direction; they also reflect whether the rupture is represented as a single curved surface, a composite source, or an interacting fault system. Tang et al. [47] combined InSAR and GNSS with Coulomb-stress calculations and attributed the main rupture to a transpressive, WNW-dipping low-angle fault associated with the Central Range fault. Their analysis further linked the sequence to stress transfer from earlier earthquakes and to the activation of neighboring structures. This extends the source-geometry debate to fault interaction, but the stress calculation is not tested by the public GNSS products analyzed here.

Recent studies have sharpened rather than removed this ambiguity. Bai et al. [10] jointly inverted seismic and geodetic observations and resolved four coseismically activated segments, including conjugate reverse faults that meet at depth. Hsu et al. [11] combined onshore and seafloor geodesy with relocated seismicity and assigned comparable geodetic moments to a steep east-dipping Longitudinal Valley fault segment and a gentler west-dipping offshore fault. Pan et al. [12] combined tsunami waveforms with InSAR and favored a west-dipping offshore tsunamigenic source, illustrating that land-based observations are least sensitive where rupture extends offshore. Yang et al. [48] used a machine-learning-enhanced earthquake and focal-mechanism catalog to resolve interaction between the Central Range and Longitudinal Valley fault systems, including a deep west-dipping structure and an east-dipping structure parallel to the Longitudinal Valley fault. Because that inference is based on seismicity and focal mechanisms rather than NGL displacements, it provides complementary structural context rather than independent validation of the GNSS field.

These published interpretations are therefore used here to provide geological context, not to select or refit a preferred fault geometry. The present analysis treats the public

GNSS field as an observational constraint whose resolved spatial pattern may be compared qualitatively with published models. It does not use the GNSS offsets to optimize model geometry, estimate slip distribution, or discriminate among the published rupture models. This distinction is important because different observation types resolve different components of the rupture, and agreement with one spatial feature does not establish a unique source model.

3. Materials and Methods

3.1. Official Coseismic Field

Official east, north, and up coseismic offsets from the NGL solution were used without rescaling or reprocessing. Horizontal and three-dimensional displacement magnitudes were calculated from the published components as:

$$H = \sqrt{E^2 + N^2}, D_{3D} = \sqrt{E^2 + N^2 + U^2} \quad (1)$$

where E, N, and U are the published east, north, and up components. Epicentral distance was calculated on a spherical Earth relative to 121.5976° E, 23.8356° N. Map coordinates were then transformed into local east and north distances in kilometers. The epicenter-centered azimuthal-equidistant projection preserves distance and azimuth from the projection center, providing a metric frame for the station-to-epicenter distances shown in the figures.

The official field provides the static reference for cross-product assessment. The USGS finite-fault patches and the regional earthquake catalog supply contextual information; neither enters the GNSS model selection. Coordinate definitions and provider-file checks are documented in Supplementary Sections S1 and S2.

3.2. Five-Minute Event-Window Offsets and Agreement Metrics

Each compressed KENV archive was read directly from the provider file. NGL labels these products as 5 Minute Final Solutions in the International GNSS Service 2020 (IGS20) reference frame. We refer to them as "5-min" or "subdaily" products rather than "high-rate" products in the strict 1-Hz sense. For each station component and each post-event window W of 1, 3, or 6 h, the event-window estimate was calculated as:

$$\hat{\delta}(W) = \text{median}_{t\in[t_0+30\text{min},t_0+W]}\, x(t) - \text{median}_{t\in[t_0-6\text{h},t_0-30\text{min}]}\, x(t) \quad (2)$$

Here t_0 is the earthquake origin time. Observations from −30 to +30 min are excluded. The pre-event window remains fixed at −6 h to −30 min, while W denotes the post-event endpoint in hours. Medians reduce sensitivity to isolated excursions. This fixed-window coordinate change can include very early post-event motion and shared processing effects; it is not an instantaneous dynamic displacement. Supplementary Sections S2 and S13 describe construction and uncertainty.

Quality grades were assigned before comparison with the official offsets. Grade A required at least 80% two-sided temporal coverage, a maximum gap of no more than 15 min, horizontal robust step uncertainty of no more than 0.020 m, and vertical robust step uncertainty of no more than 0.040 m. Grade B required at least 60% coverage, a maximum gap of no more than 30 min, and horizontal and vertical robust step-uncertainty limits of 0.040 and 0.080 m, respectively. The horizontal criterion uses the larger of the east and north step uncertainties. Grade C records were retained in the complete result tables but were not included in the principal agreement statistics. Grade D records were retained for audit purposes only and were excluded from the principal agreement analysis. The

primary comparison therefore uses grades A–B together with the complete station-level results reported separately.

For each component and event window we calculated Pearson correlation, ordinary least squares (OLS) regression, orthogonal distance regression (ODR), bias, mean absolute error (MAE), root mean square error (RMSE), and concordance. ODR uses the official component uncertainty as the predictor standard deviation and the robust event-window step uncertainty as the response standard deviation. The latter is the square root of the sum of the pre- and post-window robust variance divided by their sample counts. Missing or non-positive uncertainties are replaced by the within-component median positive uncertainty, with a documented fallback. The ODR point fit uses a diagonal errors-in-variables approximation and does not estimate cross-product covariance. Lin's concordance correlation coefficient (CCC) measures association and departure from the one-to-one relation:

$$\rho_c = \frac{2\sigma_{xy}}{\sigma_x^2 + \sigma_y^2 + (\mu_x - \mu_y)^2} \quad (3)$$

Bland–Altman differences and limits are descriptive because both products inherit shared observations and processing. To assess sensitivity to spatial dependence, 1000 bootstrap samples resample complete 0.5° latitude–longitude blocks of stations, preserving the two product values and uncertainties within each selected block. The six-hour sample occupies 21 blocks. Percentile intervals from this diagnostic replace station-independent errors as the main uncertainty qualification (Figure S8a). Block resampling captures local clustering only approximately and does not remove shared orbit, reference-frame, or network-wide errors. ODR is therefore a conditional consistency analysis, rather than independent validation.

3.3. Daily-Series Preparation

For each TENV3 component, a station-specific pre-event trend was fitted over days −210 to −2. Robust prescreening removed residuals exceeding the larger of 0.03 m and five robust standard deviations during trend estimation. The fitted trend was extrapolated into the post-event interval and subtracted. The official coseismic component was then removed, and the residual series was referenced to the median of post-event days 1–3. Integer post-event day labels were used to select the reference interval, while fitting retained the actual elapsed times relative to the earthquake origin. Before constructing a component series, at least 10 residual observations were required between days −30 and −2, and at least three observations were required between days 1 and 7. Model fitting additionally required at least eight observations between days 1 and 14. These requirements determine the retained station set described in Section 2.1 and Figure 1.

Reference sensitivity uses day 1, days 1–2, days 1–3, and the unshifted pretrend extrapolation. A constant shift mainly changes the intercept of these models. Short-trend sensitivity uses 120-, 180-, and 210-day windows. An additional background fit uses days −1095 to −2 with a linear trend, annual and semiannual harmonics, and steps at documented provider discontinuity dates. At least 400 pre-event observations and a full-rank design are required. This longer-window fit is a background diagnostic, not a calibrated hydrological loading correction. Known equipment changes are audited using the downloaded NGL discontinuity catalog; no type-1 equipment change is documented during the retained post-event interval. A leave-target-station-out median stack from stations at least 100 km from the epicenter provides a separate common-mode sensitivity test. It requires at least ten reference stations at each daily epoch and can remove genuine broad deformation as well as processing noise. Details and limitations are given in Supplementary Sections S3 and S4; background examples are shown in Figure S7.

3.4. Empirical Models and Likelihood-Consistent AICc

The corrected Akaike information criterion (AICc) is used to compare four empirical descriptions: a constant, a linear drift, a logarithmic curve, and an exponential curve. The added linear alternative separates changing coordinates from resolved curvature:

$$d(t) = c \tag{4}$$

$$d(t) = c + v(t - t_{\min}) \tag{5}$$

$$d(t) = c + A\ln\left(1 + \frac{t}{\tau}\right) \tag{6}$$

and

$$d(t) = c + A\left[1 - \exp\left(-\frac{t}{\tau}\right)\right] \tag{7}$$

Here c is a level, v is a linear rate, A is an empirical amplitude, and τ lies between 0.1 and 60 days. The linear model uses time centered on the first retained epoch. Nonlinear intercepts and amplitudes are bounded to ± 0.5 m. A profile fit evaluates 161 logarithmically spaced τ values and solves the weighted bounded intercept/amplitude problem at each value; the same fitting algorithm is used for observed, bootstrap, and null records. A 641-point grid checks candidate classification. Fits with τ within 5% of either bound or an intercept/amplitude within 10% of its bound are flagged to avoid grid-sensitive near-bound solutions. These warning margins are numerical diagnostics, rather than data-derived physical limits; classification near a bound is additionally checked on a finer grid.

Models were fitted by weighted least squares using the reported daily coordinate uncertainties as relative standard deviations. The same weights were used for fitting and model ranking. To maintain consistency with the likelihood calculation, the residual scale s was estimated as a multiplicative parameter in the concentrated Gaussian likelihood:

$$-2\ln L = n\left[\ln(2\pi) + 1 + \ln\left(\frac{1}{n}\sum_{i=1}^{n}\left(\frac{y_i - f_i}{\sigma_i}\right)^2\right)\right] + 2\sum_{i=1}^{n}\ln\sigma_i \tag{8}$$

The residual scale s is counted as an estimated parameter; n is the number of retained observations and K is the total number of estimated parameters. Consequently $K = 2$ for the constant model, $K = 3$ for the linear model, and $K = 4$ for the logarithmic and exponential models. AICc is finite only when $n > K + 1$. The revised four-model comparison requires at least six observations for the seven-day diagnostic and at least eight for the ten- and fourteen-day comparisons. The three observations during days 1–7 in preprocessing constitute an eligibility check, not the sample count used for AICc. Records below the relevant fitting minimum are labeled not estimable, and no nonlinear AICc is calculated for $n \leq 5$. Small-sample ranking uses

$$\mathrm{AICc} = -2\ln L + 2K + \frac{2K(K+1)}{n - K - 1} \tag{9}$$

Support for any nonconstant behavior is measured by the constant AICc minus the minimum across all four models. Values no greater than two are unresolved [49–51]. Curvature is evaluated separately as the minimum AICc among constant/linear models minus the minimum among logarithmic/exponential models. A positive difference greater than two favors a curved description within this candidate set. These are relative model-support criteria, not frequentist significance tests or evidence identifying a physical mechanism.

An intermediate-screen candidate has support over a constant greater than two AICc units, no near-bound warning, and absolute fitted change over the observed interval no greater than 0.15 m. The linear model can pass this screen without a time constant.

Nonlinear A and τ are reported as empirical parameters, while curvature support is reported separately. All model scores, exclusions, bounds, and grid diagnostics appear in Tables S3 and S11.

3.5. Robustness and Null Simulations

The four-model candidate screen is repeated for four references, weighted/unweighted fits, seven-, ten-, and fourteen-day post-event windows, and 120-, 180-, and 210-day pre-event trends. Leave-one-out tests omit each observed daily position in turn. Five hundred residual-bootstrap records are generated for each intermediate-screen candidate from centered standardized residuals of its selected model. All four models are refitted in every replicate; candidate-model uncertainty is therefore included in this conditional resampling diagnostic. Bootstrap retention and curve bands are conditional diagnostics because residual draws are exchangeable and do not preserve the complete colored-noise process.

A conditionally retained component passes the intermediate screen, is retained for at least three of four references, remains screened without weights, is retained in at least two eligible post-event windows and two pretrend windows, and reaches 0.80 retention in both leave-one-out and bootstrap tests. Post-window eligibility and the denominator are reported separately. Seasonal/step and common-mode diagnostics form an additional reported check, rather than retrospectively being described as prespecified tests. These conditions assess stability under the specified choices and do not themselves calibrate statistical significance.

One thousand constant-signal networks test the intermediate four-model screen. Simulated noise uses first-order autoregressive [AR(1)] coefficient $\varphi = 0.4$ and common-mode amplitude coefficient $\gamma = 0.25$, equivalent to a 6.25% marginal-variance contribution. The common process is aligned by actual post-event day across stations, and each component retains its observation dates, formal-uncertainty pattern, and constant-fit residual scale. The same profile grid, model set, parameter warnings, and amplitude screen are applied to observations and simulations.

The plus-one-corrected exceedance probability calibrates only the number of intermediate-screen candidates under this specified noise scenario. Reference/window/trend tests, leave-one-out, residual bootstrap, and the added background diagnostics are not applied as a complete final-selection pipeline to the null networks. Accordingly, the final retained count has no calibrated network false-selection probability in this study. Neither an individual retained component nor the final count is described as statistically significant. φ and γ are sensitivity assumptions, not estimates of the full NGL covariance or noise spectrum.

3.6. Reproducibility and Validation

The revised provider-file-to-result workflow, four-model statistics, diagnostic metadata, figures, and automated validation accompany this article in ESM_3.zip. The current numerical workbook ESM_2.xlsx includes every comparison, retention fraction, uncertainty interval, and intermediate null-network count. Validation checks input hashes, sample eligibility, the evidence partition, the AICc parameter counts, and grid convergence; these checks establish computational consistency rather than the physical truth of selected changes.

4. Results

4.1. Coseismic Displacement Field

The official NGL product contains 105 three-component offsets and supplies the static reference field (Figure 2; Table 2). Its maximum horizontal displacement is 0.262 m at

HUAP, while HUA3 has the maximum vertical component, 0.440 m, and maximum three-dimensional norm, 0.448 m. Signed components and vector norms are retained separately. These are descriptive provider-product results; the original contribution evaluated below is their recovery from five-minute records and the limits of short daily-coordinate inference.

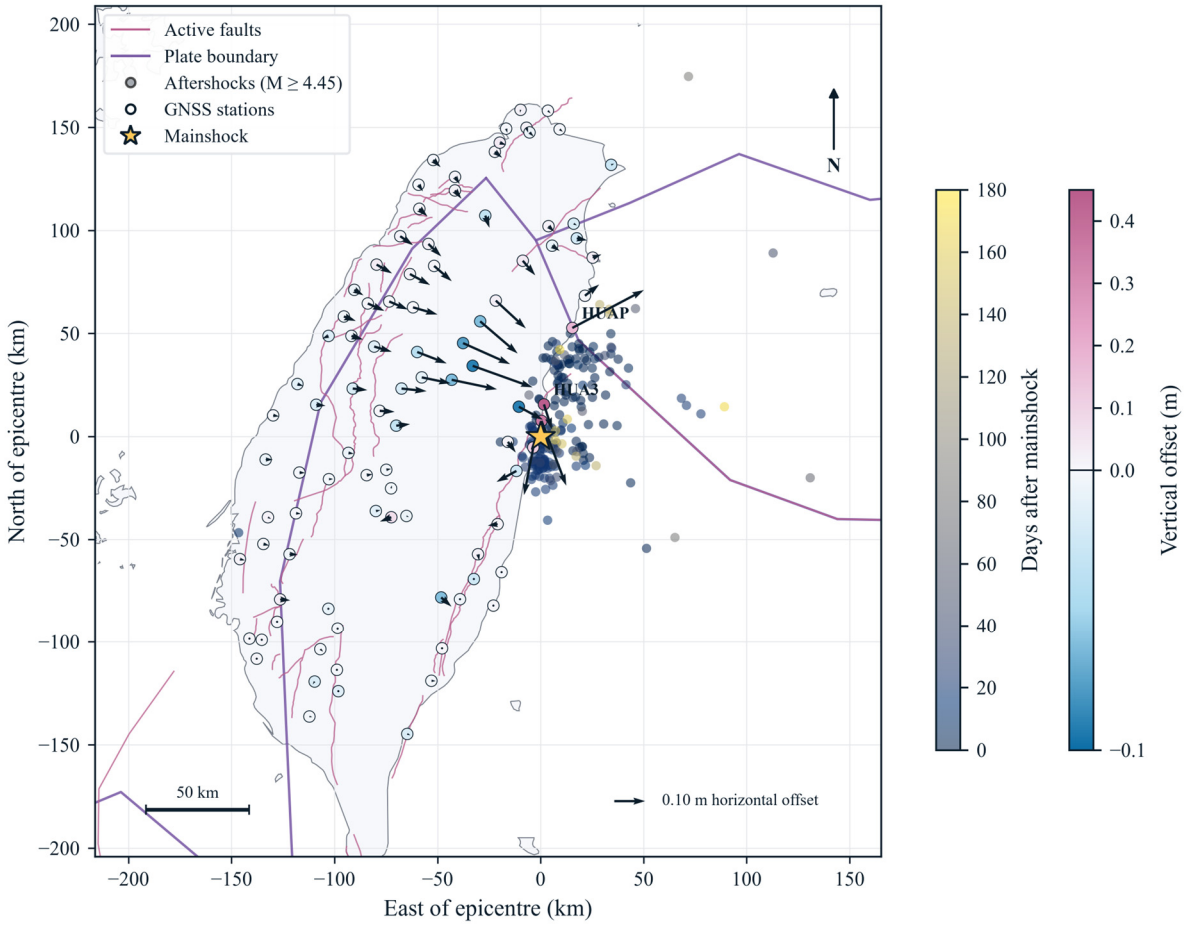


Figure 2. Official Nevada Geodetic Laboratory (NGL) coseismic displacement field in an azimuthal-equidistant frame centred on the epicentre. Arrows show horizontal displacement, and station color represents the signed vertical component. The reference arrow denotes 0.10 m of horizontal displacement. Earthquakes with $M \geq 4.45$ are colored by elapsed time after the mainshock and are included only as regional context. Active faults, plate boundaries, coastlines, scale bar, north arrow, and selected station labels provide geographic orientation. The earthquake catalog does not enter the Global Navigation Satellite System (GNSS) analysis.

Table 2. Stations with the eight largest three-dimensional displacements in the official NGL coseismic solution. *E*, *N*, and *U* denote east, north, and up displacements, respectively.

Station	Distance (km)	*E* (m)	*N* (m)	*U* (m)	Horizontal (m)	3-D (m)
HUA3	15.6	0.026	−0.081	0.440	0.085	0.448
YENL	7.6	0.080	−0.209	0.358	0.224	0.423
HUAP	54.9	0.232	0.123	0.173	0.262	0.314
HUAN	47.6	0.194	−0.069	−0.090	0.206	0.225
SHUL	6.4	−0.030	−0.154	0.118	0.157	0.197
JYAN	58.9	0.152	−0.068	−0.076	0.167	0.183
HNSN	63.1	0.121	−0.104	−0.062	0.160	0.171
MFEN	51.2	0.147	−0.031	−0.063	0.150	0.163

The reference field is heterogeneous in direction and magnitude. Large uplift at HUA3 and YENL coexists with negative vertical offsets at several other eastern stations. The unequal component proportions motivate separate east, north, and up agreement metrics and caution against representing the network by one maximum displacement or epicentral distance alone.

The finite-fault overlay is relocated to Figure S1 because it provides geographic context rather than a forward-model test. Table 3 summarizes the observation types and source interpretations of previous studies. No numerical misfit is assigned between GNSS vectors and fault slip, radar line-of-sight displacement, or sea-surface uplift; those quantities require different observation operators.

Table 3. Published rupture interpretations and their use as contextual constraints in this study. GNSS: Global Navigation Satellite System; InSAR: interferometric synthetic aperture radar; LOS: line of sight; USGS: U.S. Geological Survey.

Study	Observations	Source Geometry	Quantity Type	Use in This Study
USGS [52]	Event source product	Provider finite-fault plane	Source slip	Qualitative spatial context
Cheloni et al. [8]	GNSS + InSAR	Composite fault	Ground motion/LOS projection	Structural context; no scalar misfit
Qiu et al. [44]	GNSS + InSAR	West-dipping	Ground motion/LOS projection	Alternative geometry
Zheng et al. [45]	Geodetic + seismic	Blind listric thrust	Source parameters and surface motion	Alternative geometry
Xu et al. [46]	Waveforms + geodesy	Conjugate faults	Source timing and slip	Multifault interpretation
Liu et al. [9]	Geodetic + seismic	Conjugate faults	Surface motion and source parameters	Multifault interpretation
Bai et al. [10]	Seismic + geodetic	Four segments	Source slip	Multisegment interpretation
Hsu et al. [11]	Onshore + seafloor geodesy	Oppositely dipping faults	Ground/seafloor displacement	Offshore sensitivity
Pan et al. [12]	Tsunami + InSAR	Offshore source	Water-surface change/LOS	Different observation operator

Onshore GNSS measures pointwise three-component motion, radar observes a projection of ground displacement, fault slip is a source parameter, and tsunami inversion constrains initial water-surface change. Published offshore and multisensor studies add information absent from this onshore product comparison [8–12]. Their source geometries are therefore discussed qualitatively, without describing unlike maxima as comparable measurements.

4.2. Cross-Product Consistency of Five-Minute and Official Offsets

The six-hour grade A–B comparison retains 69 stations for all three components (Table 4; Figure 3a–c). ODR point slopes remain 0.914 east, 1.007 north, and 0.962 up, and CCC values remain 0.844, 0.980, and 0.922. These unchanged point estimates reflect the original product comparison. Spatial-block 95% slope intervals are 0.846–0.995, 0.968–1.088, and 0.865–3.537, respectively. The broad vertical interval indicates sensitivity to resampling the spatially clustered high-amplitude stations and qualifies the near-unit point slope. North has the smallest RMSE, 0.006 m, compared with 0.019 m east and 0.028 m up.

Table 4. Six-hour grade A–B cross-product agreement, including spatial-block bootstrap slope intervals. *n*: number of paired stations; ODR: orthogonal distance regression; CI: confidence interval; CCC: concordance correlation coefficient; RMSE: root mean square error; BA: Bland–Altman. Bias and BA differences are event-window minus official estimates.

Component	*n*	ODR Slope; Block 95% CI	CCC	Bias (m)	RMSE (m)	BA Lower (m)	BA Upper (m)
East	69	0.914; 0.846–0.995	0.844	−0.001	0.019	−0.039	0.036
North	69	1.007; 0.968–1.088	0.980	0.001	0.006	−0.011	0.012
Up	69	0.962; 0.865–3.537	0.922	−0.007	0.028	−0.061	0.046

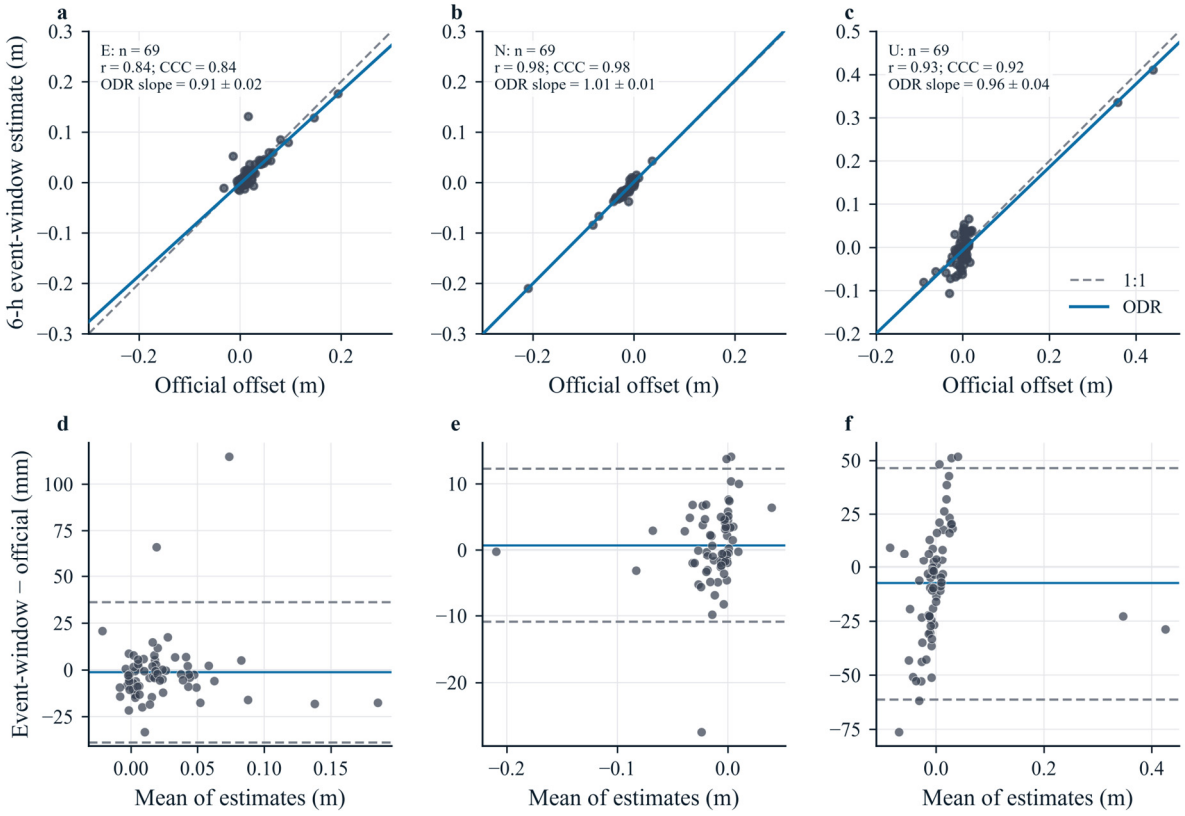


Figure 3. Cross-product consistency for six-hour grade A–B records. In (**a**–**c**), each point represents one station for the east, north, or up component, respectively; horizontal and vertical bars show the official and event-window standard uncertainties. The dashed gray line denotes equality, and the solid blue line is the orthogonal distance regression (ODR) point fit. In (**d**–**f**), each point shows the event-window minus official difference against the mean of the two estimates for the corresponding component. The solid blue horizontal line denotes the mean difference, dashed gray lines denote the descriptive 95% Bland–Altman limits, and the pale solid line marks zero difference. *n* denotes the number of paired stations, *r* is Pearson's correlation coefficient, and CCC is the concordance correlation coefficient. Point-fit errors assume diagonal uncertainties; spatial-block uncertainty is reported in Table 4 and Figure S8a. The products share observations and processing.

The Bland–Altman limits further show that the component with the highest correlation is not necessarily the only component requiring examination for absolute disagreement. The 95% descriptive limits are −0.039 to 0.036 m for east, −0.011 to 0.012 m for north, and −0.061 to 0.046 m for up (Table 4; Figure 3d–f). The larger east and up ranges are influenced by a small number of stations with appreciably greater differences than the central concentration of the data. The up component has the widest interval, consistent with its larger RMSE and the greater scatter visible around the one-to-one relation. These limits describe the observed distribution of differences; they are not inferential limits for two independent measurement

systems because the two products share station observations and elements of the NGL processing chain. Window-specific quality grades, station-level estimates, and differences are provided in Table S2a; aggregated agreement diagnostics are provided in Table S2b. These are the worksheets "Table S2a 5min" and "Table S2b agreement", respectively, in ESM_2.xlsx. Time-window sensitivity is summarized in Figure S2, and spatial-block slope uncertainty is shown in Figure S8a.

Agreement depends on the post-event window and the qualifying station set. For grade A–B records, CCC values for the 1-, 3-, and 6-h windows are 0.359, 0.626, and 0.844 for east; 0.935, 0.932, and 0.980 for north; and 0.837, 0.864, and 0.922 for up. These comparisons use 82, 84, and 69 qualifying stations, respectively (Table S2b; Figure S2). The generally closer agreement for longer windows therefore reflects both window length and changes in the qualifying station set. Representative 5-min records at HUA3, HUAN, CHUN, and SGUN illustrate why the window length matters (Figure 4). Each record resolves a coordinate step near the earthquake origin time, but short-period scatter and continued variation after the excluded ±30-min interval affect the median over the shorter windows. These examples demonstrate product-level recovery of the sign and approximate amplitude of the offset while also showing that a fixed-window estimate is not an instantaneous dynamic displacement. Because the 5-min and official products are not independent, the observed correspondence is interpreted as cross-product consistency rather than independent validation.

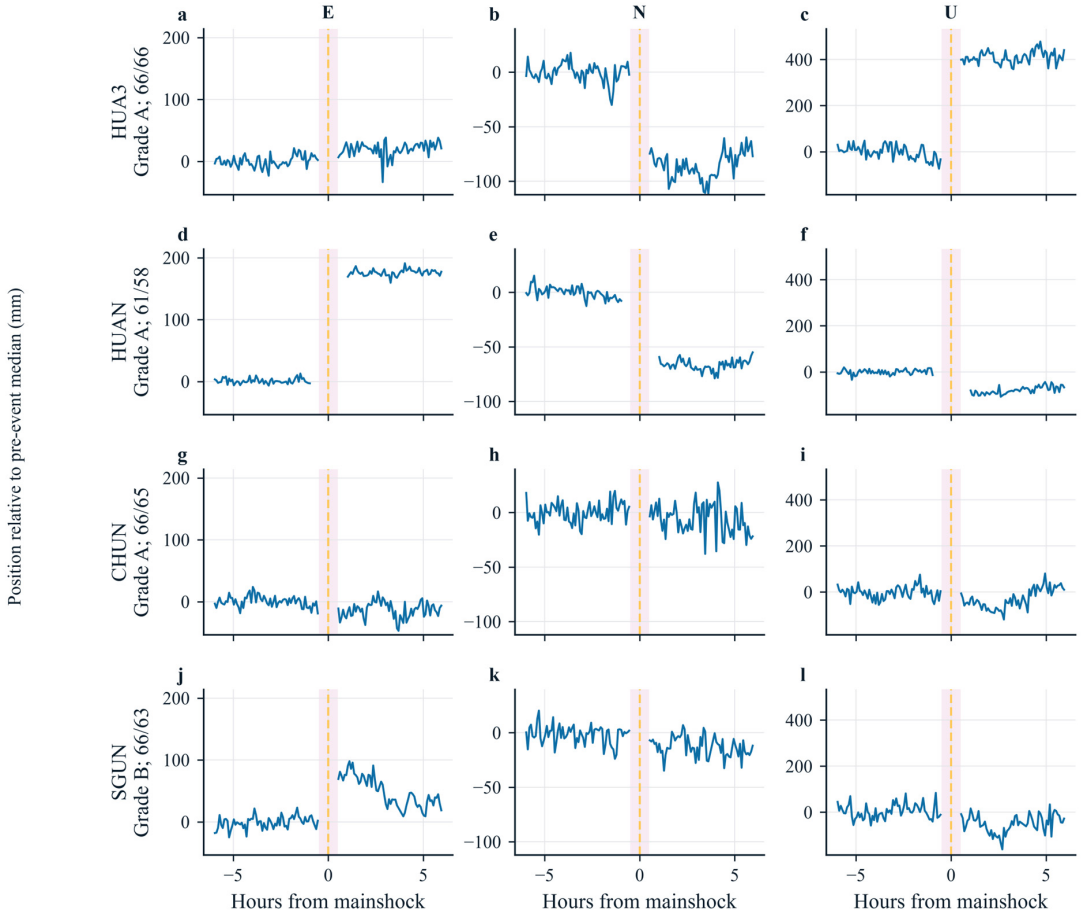


Figure 4. Five-minute positions relative to the pre-event median. Subfigures (**a**–**c**) show HUA3 east, north, and up; (**d**–**f**) HUAN east, north, and up; (**g**–**i**) CHUN east, north, and up; and (**j**–**l**) SGUN east, north, and up. The dashed line marks the origin time and shading marks the excluded ±30 min. Traces are not connected across the exclusion interval. Quality grades reflect coverage, gaps, and robust step uncertainty.

4.3. Nonconstant Variation and Curvature in the Revised Daily Comparison

Representative daily-coordinate series and fitted descriptions are shown in Figure 5. Across 300 components, minimum-AICc models are constant for 209, linear for 74, logarithmic for five, and exponential for 12 (Figure 6a). Of the 91 nonconstant best fits, 34 remain within two AICc units of a constant. The remaining 57 favor nonconstant behavior; 6 are flagged and 51 pass the intermediate screen (Table S3; Figure S3). Only 5 screened components favor curvature by more than two AICc units relative to the best constant/linear alternative (Figure 6b). The linear control clarifies the scientific interpretation: support for varying coordinates is more widespread than support for an identifiable curved transient.

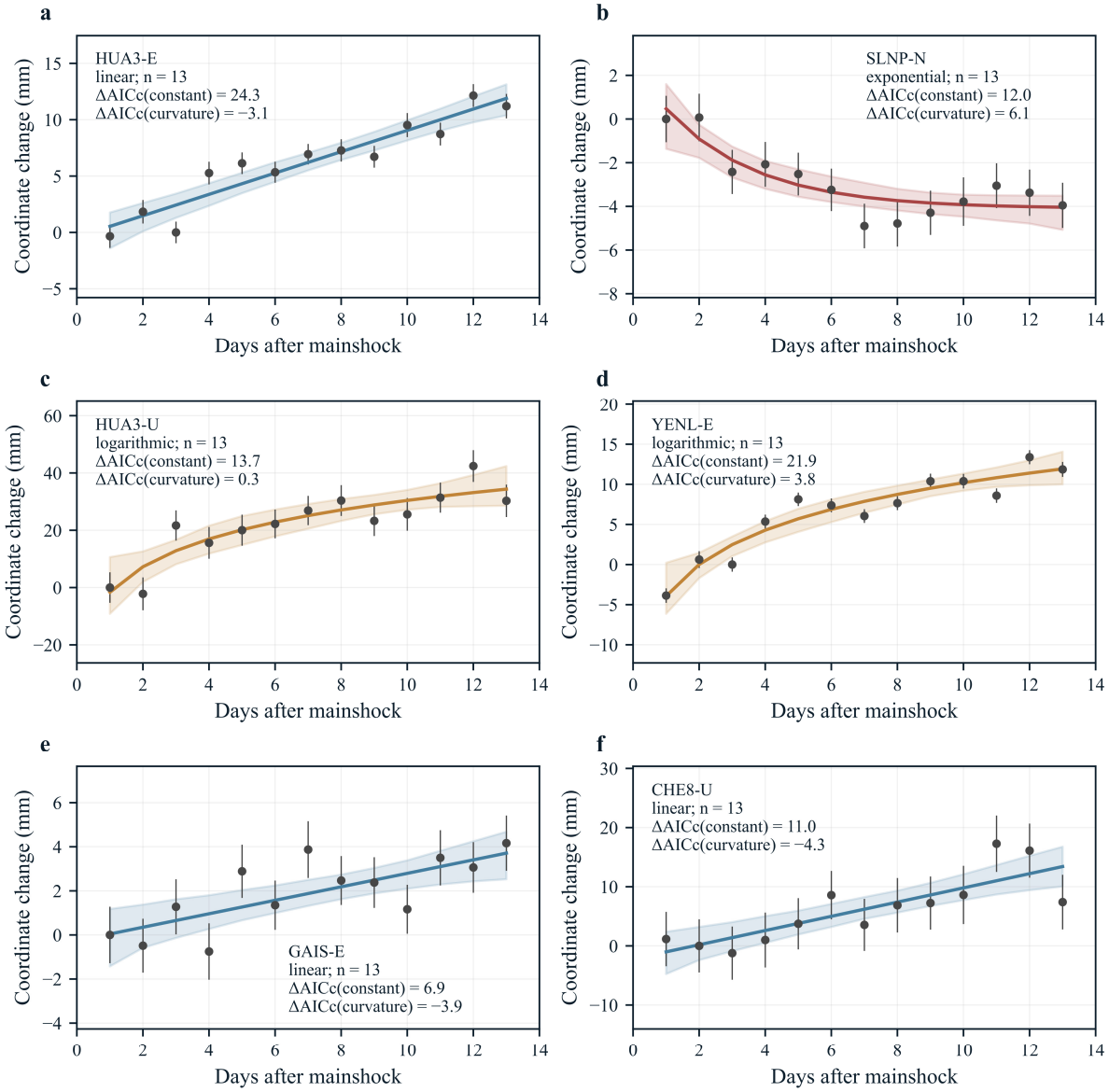


Figure 5. Daily-coordinate examples: (**a**) HUA3 east, (**b**) SLNP north, (**c**) HUA3 up, (**d**) YENL east, (**e**) GAIS east, and (**f**) CHE8 up. Points and bars show positions and formal uncertainties. Curves show the best of four models under the corrected Akaike information criterion (AICc); shading gives pointwise 95% conditional residual-bootstrap bands from refitting all models. Annotations give AICc differences (ΔAICc) against a constant and for curvature against a constant/linear alternative; *n* is sample size. Changes are referenced to days 1–3.

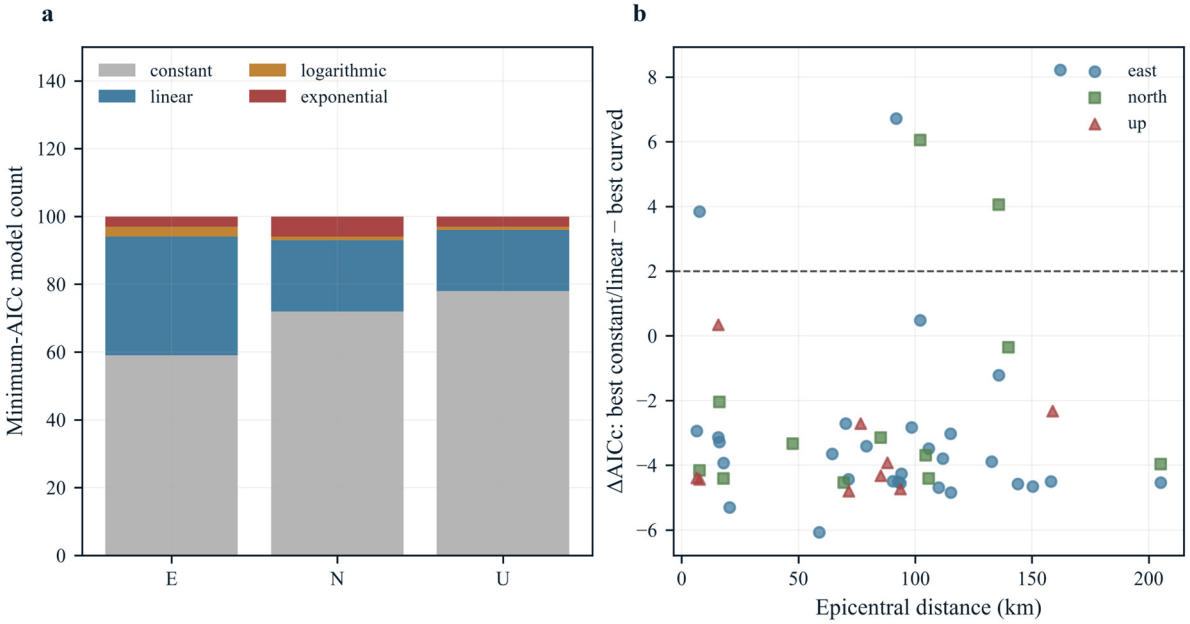


Figure 6. Revised model ranking and curvature support. (**a**) Counts of the minimum-AICc model for each component: constant, linear, logarithmic, or exponential. These counts sum to 300 and include unresolved and flagged fits. (**b**) Curvature support for intermediate-screen candidates against epicentral distance; marker shape and color identify component and the dashed line marks two AICc units. The plot does not infer a spatial deformation surface or a physical relaxation mechanism.

HUA3 east is best described by a linear model, with ΔAICc against a constant of 24.28 and curvature support of −3.14. Its observed-window fitted change is 11.36 mm. SLNP north remains exponential, with ΔAICc against a constant of 11.98, curvature support of 6.05, and fitted change of −4.51 mm. HUA3 up has a logarithmic minimum-AICc fit but lies only 0.35 AICc units below the best constant/linear alternative, so its curvature is unresolved. Figure 5 also includes examples illustrating weaker background stability and changing model support. The bands describe conditional variability after refitting all four models, not uncertainty on a deformation mechanism.

The revised intermediate screen contains 30 east, 12 north, and 9 up components. The composition depends on the tested model set, sampling, and screening diagnostics. Network-median formal daily uncertainties are 1.16, 1.04, and 5.38 mm for east, north, and up, while robust first-fortnight residual scatters are 1.65, 1.41, and 5.54 mm (Figure S8b; Table S10). Vertical noise is approximately four to five times larger than horizontal noise, making unequal detection sensitivity a plausible contributor to the horizontal predominance. These diagnostics do not establish a physical preference for horizontal post-event deformation. No retained station has all three components passing the extended checks, and individual components are not reconstructed as complete vectors.

4.4. Sensitivity, Bootstrap Uncertainty, and False Selections

The seven-, ten-, and fourteen-day four-model comparisons screen 9 of 294, 26 of 291, and 51 of 300 estimable components, respectively (Table 5; Figure S4a). Six, nine, and zero components fail the relevant minimum-sample rule and are reported separately. Thus a missing fit is not counted as observed absence of variation. Short linear-background windows of 120, 180, and 210 days screen 55, 52, and 51 components. The three-year seasonal/step diagnostic screens 51 and the common-mode diagnostic screens 36 (Figure S4b); equal aggregate counts need not mean identical component sets. Background and epoch sensitivity are retained as explicit qualifications.

Table 5. Revised four-model screen, eligibility, background sensitivity, and conditional retention. *n*: number of retained observations; LOO: leave-one-out; log: logarithmic; exp: exponential; *P*: exceedance probability.

Analysis Factor	Setting	Result
Four-model comparison	Constant/linear/log/exp best	209/74/5/12
Nonconstant evidence	Unresolved/supported	34/57
Intermediate screen	Pass/flagged	51/6
Curvature support	Against best constant or linear	5
Post-event window	7/10/14 days	9/294; 26/291; 51/300
Fit eligibility	Minimum *n* for 7/10/14 days	6/8/8
Linear pretrend	120/180/210 days	55/52/51
Background controls	Seasonal + steps/common mode	51/36
Conditional stability	Reference + weighting + windows + LOO + bootstrap	15
Extended diagnostics	Also seasonal + steps and common mode	10
Intermediate null	$P(\text{count} \geq \text{observed})$	0.2547
Final-selection null	Complete retention procedure	Not calibrated

Fifteen intermediate-screen components satisfy the reference, weighting, eligible-window, short-trend, leave-one-out, and bootstrap conditions. Ten of these also retain screened status under both additional background diagnostics (Table S4; Figure S6). Among these ten, only SLNP north has curvature support greater than two in the baseline four-model comparison. HUA3 east illustrates a reproducible fitted change whose linear description is sufficient. HUA3 up illustrates a curved best fit without resolved curvature relative to a linear alternative. The ten-component result is conditional on the tested analysis choices; the selection procedure is not calibrated under the complete final null pipeline.

For 1000 null networks the intermediate-screen count has mean 45.75 and 95th percentile 59. The observed count of 51 has a plus-one-corrected exceedance probability of 0.255 under the specified AR(1)/common-mode scenario (Figure S5; Table S5). This result applies to the intermediate screen only. No corresponding probability is available for the ten components retaining status after all descriptive stability and background checks. Final retention is therefore not interpreted as statistical significance or full null calibration. The bootstrap and sensitivity results characterize conditional stability and cannot replace calibration of the full final-selection procedure.

5. Discussion

5.1. What the Public Products Resolve Well

The strongest result of this study is the product-level coseismic displacement field. The official NGL offsets resolve centimeter- to decimeter-scale displacement variations across the 105-station network, including substantial horizontal and vertical components near the source region and clear changes in displacement direction across Taiwan (Figure 2; Table 2). HUA3 has the largest three-dimensional displacement, 0.448 m, whereas HUAP has the largest horizontal displacement, 0.262 m, and HUA3 has the largest individual vertical component, 0.440 m. These different maxima show that the observed field cannot be summarized by a single scalar amplitude or by epicentral distance alone. The public static solution therefore provides a reproducible observational constraint on the sign, scale, and first-order spatial heterogeneity of the coseismic displacement field.

The five-minute agreement hierarchy concerns product-specific recovery: north has the smallest absolute discrepancy, while east and up have larger window and spatial-sampling sensitivity. The comparison uses paired products rather than independent observations. A short-window coordinate difference can combine static motion, early variation, and

processing effects. The spatial-block result further cautions that a point slope near one need not have a narrow uncertainty interval.

The products contribute different temporal information. Official offsets provide the static reference, five-minute positions allow event-window consistency checks, and daily coordinates support comparison of constant, linear, and curved descriptions. ODR, concordance, absolute differences, and spatial-block diagnostics qualify recovery from the subdaily product (Figure 3; Supplementary Sections S2 and S13). Model ranking and background diagnostics qualify daily-coordinate variation.

Cross-product comparison is not independent validation. The official offsets and the 5-min KENV series share station observations and elements of the NGL processing chain. Their agreement therefore demonstrates operational consistency within related public products rather than agreement between independent measurement systems. This distinction is important for interpreting the strong north-component concordance and the lower east- and up-component agreement. A high correlation can coexist with a scale bias or a non-negligible absolute difference, whereas ODR, CCC, and Bland–Altman limits explicitly expose these departures from the one-to-one relation. The practical contribution of this comparison is consequently methodological: it establishes what can be reproduced from public products at different temporal resolutions without overstating the independence of the comparison.

5.2. Relation to Published GNSS–InSAR Rupture Studies

Published GNSS–InSAR and joint source studies provide complementary information about the rupture [8–12,44–48]. The literature comparison is now restricted to observation types, inferred geometry, and offshore sensitivity. GNSS vector norms are not compared numerically with radar line-of-sight displacement, source slip, or initial sea-surface elevation. Table 3 makes these distinctions explicit.

Published studies reach different structural interpretations because they combine different observation types and impose different parameterizations. Cheloni et al. [8] used GNSS and InSAR to infer a composite source and reported approximately 0.40–0.45 m of maximum line-of-sight deformation near Hualien. Qiu et al. [44] favored a west-dipping structure from InSAR and GNSS, whereas Zheng et al. [45] inferred a blind listric, southeast-dipping thrust. Xu et al. [46] and Liu et al. [9] supported conjugate or multiple-fault participation, and Bai et al. [10] resolved four coseismically activated segments from joint seismic-geodetic inversion. Hsu et al. [11] combined onshore and seafloor geodesy with relocated seismicity and assigned comparable geodetic moments to a steep east-dipping Longitudinal Valley fault segment and a gentler west-dipping offshore fault. Pan et al. [12] used tsunami waveforms and InSAR to favor a west-dipping offshore tsunamigenic source. These studies should not be treated as redundant alternatives that can be discriminated against by comparing peak displacement values alone. Their differences reflect observation geometry, offshore sensitivity, data weighting, fault parameterization, and the partitioning of slip among interacting structures.

Radar, land and seafloor GNSS, seismic waveforms, and tsunami observations constrain different observation operators. Their complementary spatial and temporal sensitivities explain why studies using different combinations can infer different source geometries. A shared earthquake context does not make the measured quantities interchangeable. This product-level analysis contributes no independent quantitative discrimination among those published geometries.

Figure S1 retains the finite-fault overlay as background rather than a main result. It shows the locations of provider patches and observed station vectors without computing

predicted GNSS motion or a residual. It is neither an elastic forward-model comparison nor a basis for selecting fault geometry.

5.3. Limits of the Early Daily Record

A first-fortnight record with 8–13 daily observations has limited ability to resolve curvature. Explicit comparison with a linear drift is crucial: logarithmic or exponential curves with long time constants can approximate a line over a short interval. The revised screen therefore separates nonconstant variation from curvature support. Eligibility also matters; an insufficient seven-day record provides no model test. Even when a linear change is reproducible, it can reflect imperfect extrapolation of a seasonal or loading signal, common-mode variation, or local site behavior. Seasonal/step and common-mode diagnostics directly test part of this background sensitivity, but do not identify its physical origin.

HUA3 east and SLNP north illustrate the distinction between coordinate variation and curvature. The former is best described by a linear drift after adding the missing control; the latter retains relative support for an exponential curve. HUA3 up, newly passing the revised conditional screen, has unresolved curvature despite a logarithmic minimum. These component results do not define a complete three-dimensional vector or source. An empirical time constant from a sparse short record is not a resolved physical relaxation time, and residual-bootstrap bands remain conditional on the fitting and resampling assumptions.

The intermediate network count is not unusual under the specified correlated-noise experiment ($p = 0.255$). Final conditional retention is a different statistic whose complete selection pipeline has not been simulated. It follows that neither the ten-component set nor SLNP north alone has a demonstrated final false-alarm rate in this study. This limitation is stated in the abstract, methods, results, and conclusions. Full calibration would have to reproduce background estimation, epoch selection, sensitivity checks, and resampling for every null realization rather than applying only the intermediate model screen.

5.4. Reproducibility, Data Dependence, and Scope of Inference

The revised workflow links provider-file hashes, preprocessing, four-model fits, eligibility, backgrounds, resampling, and intermediate null records to current figures and tables. Supplementary Sections S1–S17 and ESM_2.xlsx document that traceability. Validation tests mathematical parameter counting, independent numerical solutions, grid convergence, eligibility, and hashes, allowing computational discrepancies to be localized without treating arithmetic consistency as physical validation.

Reproducibility and statistical independence answer different questions. ODR uses the reported marginal uncertainties, and spatial-block resampling reveals sensitivity to local station clustering, but neither captures the complete joint covariance of shared NGL products. The wide vertical slope interval cautions against interpreting a near-unit point estimate as precise independent agreement. Likewise, harmonic detrending represents predictable seasonal structure but does not provide a physically modeled hydrological loading correction. Documented discontinuities are included where estimable, while undocumented steps and past-event nonlinear tails can remain in the background residual.

The regional earthquake catalog supplies map context and is not used for an Omori fit, Coulomb stress estimate, or joint inference of seismicity and coordinate change. No long-duration displacement is extrapolated from the first-fortnight record. Longer independently processed observations could test the persistence and spatial coherence of the conditionally retained components and allow explicit covariance/loading treatment. Attribution to afterslip or another mechanism would additionally require a physically parameterized source model.

The transferable methodological result is the need for explicit controls before interpreting a short public GNSS series. A linear alternative separates drift from curvature; an eligibility audit distinguishes an untestable record from a negative result; background diagnostics reveal dependence on the pre-event model; and spatial resampling qualifies apparent cross-product agreement. These checks improve interpretation without implying a new rupture or relaxation model.

6. Conclusions

Public NGL products supply a heterogeneous coseismic reference field for the Hualien earthquake, including maximum horizontal, vertical, and three-dimensional values of 0.262, 0.440, and 0.448 m. Those descriptive provider quantities are kept distinct from radar line-of-sight observations and source-model parameters. Fixed-window five-minute estimates recover the main sign and amplitude pattern, providing useful consistency information within the shared processing lineage.

The six-hour comparison has CCC values of 0.844, 0.980, and 0.922 for east, north, and up. North has the lowest absolute discrepancy; east and up are more sensitive to window and station selection. Spatial-block bootstrap intervals, particularly the broad vertical interval, show that diagonal ODR errors alone understate an important source of uncertainty. The reported agreement remains product-specific and conditional on the assumed marginal uncertainties.

The revised four-model comparison screens 51 of 300 daily components, but only 5 support curvature over a constant/linear alternative. Fifteen meet the tested stability conditions, and ten retain screened status under added seasonal/step and common-mode diagnostics. These are conditionally retained coordinate changes, not complete station vectors, a validated regional postseismic field, or a unique physical mechanism. The correlated-noise exceedance probability of 0.255 calibrates the intermediate count only; no final-pipeline false-selection probability is claimed. Longer records, empirically estimated covariance, and complete final-selection calibration are needed before stronger physical or statistical attribution.

Supplementary Materials: The following supporting information can be downloaded at: https://www.mdpi.com/article/10.3390/app162110575/s1. The supplementary files are ESM_1.pdf, ESM_2.xlsx, and ESM_3.zip. ESM_1.pdf contains Supplementary Sections S1–S17 and the following figures. Figure S1: contextual finite-fault overlay; Figure S2: five-minute agreement sensitivity for one-, three-, and six-hour subsets; Figure S3: four-model support for nonconstant variation against epicentral distance; Figure S4: record-window eligibility and background-screening sensitivity; Figure S5: intermediate-screen counts from correlated-noise null networks; Figure S6: retention diagnostics for the 51 intermediate-screen candidates, displayed in two parts; Figure S7: linear versus seasonal/step background examples; Figure S8: spatial-block slope intervals and component-noise diagnostics. ESM_2.xlsx supplies 18 worksheets: Table S1: official offsets; Table S2a: five-minute station estimates and quality grades; Table S2b: aggregate agreement; Table S3: baseline/background model fits; Table S4: sensitivity, conditional retention, leave-one-out, and bootstrap records; Table S5: intermediate-null networks and component outputs; Table S6: backgrounds; Table S7: raw-data provenance; Table S8: documented discontinuities; Table S9: spatial-block regression; Table S10: component precision and noise; Table S11: grid convergence. ESM_3.zip supplies the full Python 3.12.14 workflow, configuration, dependencies, outputs, editable figures, tests, validation reports, and frozen inputs (data/raw/Public_GNSS_Hualien_data). Recorded package versions are NumPy 2.3.5, pandas 3.0.1, SciPy 1.18.1, and Matplotlib 3.11.1. SUPPLEMENTARY_FILE_INDEX.md maps figures and tables to files; documentation/Supplementary_Information.docx is the editable ESM_1.pdf source. Original provider filenames and hash manifests are preserved; third-party terms apply.

Author Contributions: Conceptualization: G.L.; Methodology: G.L.; Software: G.L.; Validation: G.L., Y.Y. and L.F.; Formal analysis: G.L., M.Z. and L.F.; Investigation: G.L.; Resources: M.Z.; Data curation: G.L.; Visualization: G.L.; Writing—original draft: G.L.; Writing—review and editing: L.F., G.L., M.Z., Y.D. and Y.Y.; Supervision: M.Z. and L.F.; Project administration: M.Z.; Funding acquisition: M.Z. All authors have read and agreed to the published version of the manuscript.

Funding: This work was supported by the National Key Research and Development Program of China (Grant 2018YFC1504700) and the National Natural Science Foundation of China (Grant 41530640), both awarded to M.Z.

Institutional Review Board Statement: Not applicable.

Informed Consent Statement: Not applicable.

Data Availability Statement: Public source products and their original filenames, retrieval information, file sizes, and SHA-256 hashes are listed in Table S7. The frozen provider archive defines the analysis version; later provider updates may differ. NGL discontinuity metadata used in the revision were downloaded on 9 October 2026 from https://geodesy.unr.edu/NGLStationPages/steps.txt and archived with URL and checksum provenance [53]. ESM_2.xlsx supplies the current station-level results. ESM_3.zip supplies the full Python workflow, dependency specifications, tests, configuration, validation records, and frozen provider inputs needed for reproduction. The code is released under the MIT License; third-party data retain their original terms. The README specifies the input layout and reproduction commands; SUPPLEMENTARY_FILE_INDEX.md identifies the current supplementary figures, table worksheets, detailed resampling records, and validation files.

Acknowledgments: Declaration of Generative AI-Assisted Technologies: AI-assisted tools supported language revision and analytical-code development. The authors take responsibility for the analyses, their verification, and the submitted manuscript.

Conflicts of Interest: The authors declare no conflict of interest.

References

1. Suppe, J. Kinematics of arc-continent collision, flipping of subduction, and back-arc spreading near Taiwan. *Mem. Geol. Soc. China* **1984**, *6*, 21–33.
2. Ho, C.S. A synthesis of the geologic evolution of Taiwan. *Tectonophysics* **1986**, *125*, 1–16. [CrossRef]
3. Teng, L.S. Geotectonic evolution of late Cenozoic arc-continent collision in Taiwan. *Tectonophysics* **1990**, *183*, 57–76. [CrossRef]
4. Rau, R.J.; Wu, F.T. Tomographic imaging of lithospheric structures under Taiwan. *Earth Planet. Sci. Lett.* **1995**, *133*, 517–532. [CrossRef]
5. Yu, S.B.; Chen, H.Y.; Kuo, L.C. Velocity field of GPS stations in the Taiwan area. *Tectonophysics* **1997**, *274*, 41–59. [CrossRef]
6. Shyu, J.B.H.; Sieh, K.; Chen, Y.G.; Liu, C.S. Neotectonic architecture of Taiwan and its implications for future large earthquakes. *J. Geophys. Res.* **2005**, *110*, B08402. [CrossRef]
7. Hsu, Y.J.; Yu, S.B.; Simons, M.; Kuo, L.C.; Chen, H.Y. Interseismic crustal deformation in the Taiwan plate boundary zone revealed by GPS observations, seismicity, and earthquake focal mechanisms. *Tectonophysics* **2009**, *479*, 4–18. [CrossRef]
8. Cheloni, D.; Famiglietti, N.A.; Caputo, R.; Tolomei, C.; Vicari, A. A composite fault model for the 2024 Mw 7.4 Hualien earthquake sequence in eastern Taiwan inferred from GNSS and InSAR data. *Geophys. Res. Lett.* **2024**, *51*, e2024GL110255. [CrossRef]
9. Liu, Z.; Hu, J.C.; Li, Z.; Yu, C.; Song, C.; Wang, Z.; Zhang, X.; Liu, H.; Han, B.; Hu, X.; et al. New insights of the conjugate seismogenic structure in the northernmost Longitudinal Valley revealed by the 2024 Hualien (Taiwan) earthquake from geodetic and seismic observations. *J. Geophys. Res. Solid Earth* **2025**, *130*, e2024JB031025. [CrossRef]
10. Bai, R.; Sang, Y.; Ding, C.; Liu, C.; Ye, L.; Lay, T.; Xiong, N.; Xiong, X. Complex rupture of the 2 April 2024 Mw 7.4 Hualien earthquake inferred from seismic and geodetic observations. *Tectonophysics* **2026**, *927*, 231141. [CrossRef]
11. Hsu, Y.J.; Wang, Y.; Tung, H.; Lin, Y.N.; Tang, C.H.; Huang, H.H.; Chen, H.Y.; Shyu, J.B.H. Complex rupture of the 2024 Mw 7.3 Hualien earthquake from onshore and seafloor geodesy and its tectonic implications. *Seismol. Res. Lett.* **2026**. *advance online publication*. [CrossRef]
12. Pan, X.; Li, L.; Shi, H.; Wang, Y.; Zhang, Z.; Feng, W.; Qiu, Q. Resolving the tsunamigenic source of the 2024 Mw 7.4 Hualien earthquake: Integrated tsunami-waveform inversion and InSAR constraints on complex multi-fault rupture. *Earthq. Res. Adv.* **2026**, 100486, *in press*. [CrossRef]
13. Mao, A.; Harrison, C.G.A.; Dixon, T.H. Noise in GPS coordinate time series. *J. Geophys. Res.* **1999**, *104*, 2797–2816. [CrossRef]

14. Dong, D.; Fang, P.; Bock, Y.; Cheng, M.K.; Miyazaki, S. Anatomy of apparent seasonal variations from GPS-derived site position time series. *J. Geophys. Res.* **2002**, *107*, 2075. [CrossRef]
15. Williams, S.D.P. The effect of coloured noise on the uncertainties of rates estimated from geodetic time series. *J. Geod.* **2003**, *76*, 483–494. [CrossRef]
16. Langbein, J. Noise in two-color electronic distance meter measurements revisited. *J. Geophys. Res.* **2004**, *109*, B04406. [CrossRef]
17. Blewitt, G.; Kreemer, C.; Hammond, W.C.; Gazeaux, J. MIDAS robust trend estimator for accurate GPS station velocities without step detection. *J. Geophys. Res. Solid Earth* **2016**, *121*, 2054–2068. [CrossRef] [PubMed]
18. Blewitt, G.; Hammond, W.C.; Kreemer, C. Harnessing the GPS data explosion for interdisciplinary science. *Eos* **2018**, *99*, e2020943118. [CrossRef]
19. Gazeaux, J.; Williams, S.; King, M.; Bos, M.; Dach, R.; Deo, M.; Moore, A.W.; Ostini, L.; Petrie, E.; Roggero, M.; et al. Detecting offsets in GPS time series: First results from the detection of offsets in GPS experiment. *J. Geophys. Res. Solid Earth* **2013**, *118*, 2397–2407. [CrossRef]
20. Tobita, M. Combined logarithmic and exponential function model for fitting postseismic GNSS time series after 2011 Tohoku-Oki earthquake. *Earth Planets Space* **2016**, *68*, 41. [CrossRef]
21. Bos, M.S.; Fernandes, R.M.S.; Williams, S.D.P.; Bastos, L. Fast error analysis of continuous GNSS observations with missing data. *J. Geod.* **2013**, *87*, 351–360. [CrossRef]
22. Langbein, J. Improved efficiency of maximum likelihood analysis of time series with temporally correlated errors. *J. Geod.* **2017**, *91*, 985–994. [CrossRef]
23. Wdowinski, S.; Bock, Y.; Zhang, J.; Fang, P.; Genrich, J. Southern California permanent GPS geodetic array: Spatial filtering of daily positions for estimating coseismic and postseismic displacements induced by the 1992 Landers earthquake. *J. Geophys. Res.* **1997**, *102*, 18057–18070. [CrossRef]
24. Dong, D.; Fang, P.; Bock, Y.; Webb, F.; Prawirodirdjo, L.; Kedar, S.; Jamason, P. Spatiotemporal filtering using principal component analysis and Karhunen-Loeve expansion approaches for regional GPS network analysis. *J. Geophys. Res.* **2006**, *111*, B03405. [CrossRef]
25. Miyazaki, S.; Larson, K.M.; Choi, K.; Hikima, K.; Koketsu, K.; Bodin, P.; Haase, J.; Emore, G.; Yamagiwa, A. Modeling the rupture process of the 2003 September 25 Tokachi-Oki (Hokkaido) earthquake using 1-Hz GPS data. *Geophys. Res. Lett.* **2004**, *31*, L21603. [CrossRef]
26. Beavan, J.; Samsonov, S.; Motagh, M.; Wallace, L.; Ellis, S.; Palmer, N. The Darfield (Canterbury) earthquake: Geodetic observations and preliminary source model. *Bull. N. Z. Soc. Earthq. Eng.* **2010**, *43*, 228–235. [CrossRef]
27. Marone, C.J.; Scholtz, C.H.; Bilham, R. On the mechanics of earthquake afterslip. *J. Geophys. Res.* **1991**, *96*, 8441–8452. [CrossRef]
28. Hsu, Y.J.; Bechor, N.; Segall, P.; Yu, S.B.; Kuo, L.C.; Ma, K.F. Rapid afterslip following the 1999 Chi-Chi, Taiwan earthquake. *Geophys. Res. Lett.* **2002**, *29*, 1754. [CrossRef]
29. Hsu, Y.J.; Simons, M.; Avouac, J.P.; Galetzka, J.; Sieh, K.; Chlieh, M.; Natawidjaja, D.; Prawirodirdjo, L.; Bock, Y. Frictional afterslip following the 2005 Nias-Simeulue earthquake, Sumatra. *Science* **2006**, *312*, 1921–1926. [CrossRef] [PubMed]
30. Bürgmann, R.; Ergintav, S.; Segall, P.; Hearn, E.H.; McClusky, S.; Reilinger, R.E.; Woith, H.; Zschau, J. Time-dependent distributed afterslip on and deep below the Izmit earthquake rupture. *Bull. Seismol. Soc. Am.* **2002**, *92*, 126–137. [CrossRef]
31. Perfettini, H.; Avouac, J.P. Postseismic relaxation driven by brittle creep: A possible mechanism to reconcile geodetic measurements and the decay rate of aftershocks, application to the Chi-Chi earthquake, Taiwan. *J. Geophys. Res. Solid Earth* **2004**, *109*, B02304. [CrossRef]
32. Perfettini, H.; Avouac, J.P. Modeling afterslip and aftershocks following the 1992 Landers earthquake. *J. Geophys. Res.* **2007**, *112*, B07409. [CrossRef]
33. Rousset, B.; Barbot, S.; Avouac, J.P.; Hsu, Y.J. Postseismic deformation following the 1999 Chi-Chi earthquake, Taiwan: Implication for lower-crust rheology. *J. Geophys. Res.* **2012**, *117*, B12405. [CrossRef]
34. Avouac, J.P. From geodetic imaging of seismic and aseismic fault slip to dynamic modeling of the seismic cycle. *Annu. Rev. Earth Planet. Sci.* **2015**, *43*, 233–271. [CrossRef]
35. Bird, P. An updated digital model of plate boundaries. *Geochem. Geophys. Geosyst.* **2003**, *4*, 1027. [CrossRef]
36. Styron, R.; Pagani, M. The GEM Global Active Faults Database. *Earthq. Spectra* **2020**, *36*, 160–180. [CrossRef]
37. MacFerrin, M.; Amante, C.; Carignan, K.; Love, M.; Lim, E. The Earth Topography 2022 (ETOPO 2022) global DEM dataset. *Earth Syst. Sci. Data* **2025**, *17*, 1835–1849. [CrossRef]
38. Angelier, J.; Chu, H.T.; Lee, J.C. Shear concentration in a collision zone: Kinematics of the Chihshang Fault as revealed by outcrop-scale quantification of active faulting, Longitudinal Valley, eastern Taiwan. *Tectonophysics* **1997**, *274*, 117–143. [CrossRef]
39. Lee, J.C.; Angelier, J.; Chu, H.T.; Hu, J.C.; Jeng, F.S.; Rau, R.J. Active fault creep variations at Chihshang, Taiwan, revealed by creep meter monitoring, 1998–2001. *J. Geophys. Res.* **2003**, *108*, 2528. [CrossRef]
40. Shyu, J.B.H.; Sieh, K.; Avouac, J.P.; Chen, W.S.; Chen, Y.G. Millennial slip rate of the Longitudinal Valley fault from river terraces: Implications for convergence across the active suture of eastern Taiwan. *J. Geophys. Res.* **2006**, *111*, B08403. [CrossRef]

41. Thomas, M.Y.; Avouac, J.P.; Champenois, J.; Lee, J.C.; Kuo, L.C. Spatiotemporal evolution of seismic and aseismic slip on the Longitudinal Valley Fault, Taiwan. *J. Geophys. Res. Solid Earth* **2014**, *119*, 5114–5139. [CrossRef]
42. Lee, S.J.; Huang, H.H.; Shyu, J.B.H.; Yeh, T.Y.; Lin, T.C. Numerical earthquake model of the 31 October 2013 Ruisui, Taiwan, earthquake: Source rupture process and seismic wave propagation. *J. Asian Earth Sci.* **2014**, *96*, 374–385. [CrossRef]
43. Lin, H.F.; Hsu, Y.F.; Canitano, A. Source modeling of the 2009 Fengpin-Hualien earthquake sequence, Taiwan, inferred from static strain measurements. *Pure Appl. Geophys.* **2023**, *180*, 715–733. [CrossRef]
44. Qiu, J.; Ji, L.; Zhu, L.; Li, Y.; Liu, C.; Zhao, Q. Coseismic deformation and seismogenic structure of the 2024 Hualien earthquake measured by InSAR and GNSS. *Earthq. Res. Adv.* **2025**, *5*, 100328. [CrossRef]
45. Zheng, A.; Yu, X.; Bai, C.; Xu, W.; Qian, J.; Zhang, W.; Chen, X. Thrust-dominated unilateral rupture of a blind listric fault associated with the 2024 Hualien earthquake. *Sci. Rep.* **2024**, *14*, 31496. [CrossRef] [PubMed]
46. Xu, L.; Meng, L.; Xu, W.; Lin, Y.-Y.; Geng, J.; Mohanna, S.; Kawamoto, G. Unzipping of the conjugate fault system during the 2024 Mw 7.4 Hualien earthquake. *Geophys. Res. Lett.* **2025**, *52*, e2025GL115218. [CrossRef]
47. Tang, X.; Guo, R.; Li, L.; Xu, Y.; Xu, J.; Zheng, Y.; Sun, H. Earthquake interactions in eastern Taiwan: Insight from the 2024 Mw 7.3 Hualien earthquake. *Seismol. Res. Lett.* **2025**, *96*, 9–18. [CrossRef]
48. Yang, H.Y.; Huang, H.H.; Wu, E.S.; Chen, H.A.; Liu, C.N.; Hsu, Y.F.; Liang, W.-T.; Ku, C.-S. An ML-enhanced earthquake catalog for the 2024 Mw 7.4 Hualien earthquake sequence: Insights into structural transition from collision to subduction in eastern Taiwan. *J. Geophys. Res. Solid Earth* **2025**, *130*, e2025JB032792. [CrossRef]
49. Akaike, H. A new look at the statistical model identification. *IEEE Trans. Autom. Control* **1974**, *19*, 716–723. [CrossRef]
50. Hurvich, C.M.; Tsai, C.-L. Regression and time series model selection in small samples. *Biometrika* **1989**, *76*, 297–307. [CrossRef]
51. Burnham, K.P.; Anderson, D.R. *Model Selection and Multimodel Inference: A Practical Information-Theoretic Approach*, 2nd ed.; Springer: New York, NY, USA, 2002. [CrossRef]
52. U.S. Geological Survey. M 7.4–15 km S of Hualien City, Taiwan: Event Page and ANSS ComCat Products. Available online: https://earthquake.usgs.gov/earthquakes/eventpage/us7000m9g4 (accessed on 19 September 2026).
53. Nevada Geodetic Laboratory. Station Discontinuity Catalog. Available online: https://geodesy.unr.edu/NGLStationPages/steps.txt (accessed on 9 October 2026).

Disclaimer/Publisher's Note: The statements, opinions and data contained in all publications are solely those of the individual author(s) and contributor(s) and not of MDPI and/or the editor(s). MDPI and/or the editor(s) disclaim responsibility for any injury to people or property resulting from any ideas, methods, instructions or products referred to in the content.